Fourier-Based Near-Field Three-Dimensional Image Reconstruction in a Multistatic Imaging Structure Using Dynamic Metasurface Antennas

Amir Masoud Molaei, Thomas Fromenteze, Shaoqing Hu, *Member, IEEE,* Vincent Fusco, *Fellow, IEEE,* and Okan Yurduseven, *Senior Member, IEEE*

***Abstract*—Due to physical layer compression, and consequently, the failure to produce uniform radiation patterns, it is not possible to develop fast Fourier-based image reconstruction algorithms using the raw measurements collected from metasurface antennas. An effective solution in the literature is a sub-wavelength sampling of the aperture. However, this solution is currently limited to a panel-to-probe model which requires a mechanical raster scan. On the other hand, existing works are based on time-division multiplexing. This means that only a single transmit/receive channel is active in each time slot. In this paper, we introduce a panel-to-panel model in a multistatic structure. Based on this model, two pre-processing (for two different individually measured signal and combined measured signal (CMS) scenarios) are derived to convert the raw measurements into the space-frequency domain. Then, by using the output data from the pre-processing stage and according to the configuration of the introduced imaging system, the range migration algorithm is adapted. The importance of the proposed solution for the CMS scenario is that, for the first time, it demonstrates the capability of using dynamic metasurface antennas diversity to achieve simultaneous data acquisition. The performance of the proposed approach is compared with state-of-art works in terms of reconstructed image quality and computational complexity using numerical simulations and analytical discussions.**

***Index Terms*—Three-dimensional image reconstruction, adapted range migration algorithm, combined measured signal, dynamic metasurface antennas, multistatic imaging.**

I. Introduction

NUMEROUS applications of microwave (300 MHz to 300 GHz) imaging in biomedical, concealed weapon detection, nondestructive testing, remote monitoring of people, etc. have led to the significant development of its hardware and software components in recent years [1-4]. Conventional imaging systems typically use an array of independent antennas [5, 6]. A mechanical or electronic raster scan (by sequentially-switched arrays) of the scene is performed to create a two-dimensional (2D) aperture in the horizontal and vertical directions [5, 6]. Although electronic scanning greatly improves data acquisition rates compared to mechanical scanning, large-aperture electronic-scanning arrays are still expensive and typically have high power consumption; because they require complex control circuitry and a large number of radio frequency components to perform a point-by-point raster scan of a scene to be imaged. In contrast, metasurface antennas exhibit a low profile, offer a drastically reduced low power consumption, and are easy to fabricate [7-9]. Furthermore, from the perspective of imaging schemes, it has been demonstrated that a frequency-diverse metasurface is able to produce a sequence of arbitrary field patterns with a low spatial correlation that can be used to acquire scene information without the need for a raster scan [10, 11]. Recently, the concept of dynamic metasurface antenna (DMA) [12], as a sample of waveguide-fed metasurfaces, has been proposed for modern computational imaging [4, 8, 13, 14]. DMAs may contain a large number of tunable metamaterial antenna elements that can be packed in small physical areas for a wide range of operating frequencies [15, 16].

In the literature, there are various techniques for image reconstruction [17-19]. It has been demonstrated that those techniques that offer a solution to the electromagnetic inverse scattering problem in the Fourier domain are much more computationally efficient than others [20, 21]. Despite the hardware advantages of metasurface antennas mentioned above, due to the physical layer compression and consequently the failure to produce uniform radiation patterns, instead of doing a point-to-point raster scan, quasi-random modes are used to probe and compress the scene information [22]. Therefore, the information received by the DMA is not capable of direct conversion on a Fourier basis and consequently does not allow the development of fast Fourier-based image reconstruction algorithms. To address this, an effective solution based on the sub-wavelength sampling of the aperture is presented in [11, 21,

This work was funded by the Leverhulme Trust under Research Leadership Award RL-2019-019. The work of Shaoqing Hu is funded by Brunel University London under Research Development Fund LBG194 and 2022/2023 Brunel Research Initiative and Enterprise Fund 12455. *Corresponding author: Amir Masoud Molaei.*

Amir Masoud Molaei, Vincent Fusco and Okan Yurduseven are with the Institute of Electronics, Communications, and Information Technology, Queen's University Belfast, Belfast BT3 9DT, U.K. (e-mails: a.molaei@qub.ac.uk; v.fusco@ecit.qub.ac.uk; okan.yurduseven@qub.ac.uk).

Thomas Fromenteze is with Xlim Research Institute, University of Limoges, Limoges 87000, France (e-mail: thomas.fromenteze@xlim.fr).

Shaoqing Hu is with the College of Engineering, Design and Physical Sciences, Brunel University London, Uxbridge UB8 3PH, U.K. (e-mail: shaoqing.hu@brunel.ac.uk).

Color versions of one or more of the figures in this article are available online at http://ieeexplore.ieee.org

23, 24], which provides the expression of measurements in the spatial domain. However, these works are based on a so-called panel-to-probe model in which a single 1D DMA on the transmitter (Tx)-side and a rectangular waveguide probe (point source) on the receiver (Rx)-side are used. Clearly, in such a scenario, it is necessary for Tx DMA and/or Rx to physically move to synthesize an electrically-large effective aperture and obtain 2D/3D images of the scene with the collected data. Such a mechanism still reduces data acquisition rates and is not suitable for real-time applications. Moreover, these works are based on time-division multiplexing. This means that only a single transmit/receive channel can be active at any instant. This can further reduce the data acquisition rate, especially when the total number of channels is large. Frequency-division [25] can be an alternative solution; however, its use may lead to a reduction of the range resolution because practically each Tx is allowed to access only a part of the total bandwidth [26]. Another method is to encode the transmitted signals in such a way that all Tx antennas can be turned on at the same time. Recently in [27, 28], a coding-based mechanism for imaging applications was provided. Although the mechanism developed in [27, 28] minimizes bandwidth and sampling rate requirements, it brings several drawbacks. Firstly, it has considerable complexity both in the Tx part (to generate orthogonal signals) and in the Rx part (to process the received signals based on multi-resolution analyses). Secondly, it was developed for, and is only applicable to, a conventional mechanical/electronic scanning structure with phased array antennas.

To address the above challenges, in this paper, we introduce, for the first time, a panel-to-panel model based on a multistatic structure and develop an efficient algorithm for 3D image reconstruction corresponding to this model. In addition, for the case where Txs are transmitting simultaneously, a solution is derived by which the receiver will be able to separate the corresponding signals of each individual Tx from the combined measured signal (CMS). In more detail, the main contributions of this paper include the following:

- Mathematical introduction of a panel-to-panel model based on multistatic structure for microwave imaging using DMAs.
- Providing a pre-processing step to convert the raw measurements collected by the above model to the spatial-frequency domain and create a specific set of aperture modes, and consequently generate input data for the image reconstruction algorithm.
- Adaptation of the range migration algorithm (RMA) according to the introduced imaging structure and output data from the pre-processing stage to reconstruct a 3D image of the scene based on fast Fourier calculations. To the best of our knowledge, this is the first time that an RMA-based algorithm is successfully developed and adopted for a multistatic DMA-based computational microwave imaging system.
- Deriving and presenting a mathematical solution for retrieving channel information individually in a CMS scenario. The novel idea here is that we use DMA diversity to achieve simultaneous data acquisition from all channels, which is significant for real-time operation. To the best of our knowledge, this is the first time that the modal diversity of DMA apertures is leveraged as an encoding mechanism to achieve simultaneous data acquisition from all channels. This can substantially improve the data acquisition rate, which is a key requirement for real-time operation.

The rest of this paper is organized as follows: Section II presents the details of the proposed approach including the system model, pre-processing procedure, 3D image reconstruction algorithm, and solution to face the CMS scenario; Section III is devoted to the presentation of simulation results and discussion; finally, a conclusion is provided in Section IV.

Notation: Throughout the paper, superscripts $(.)^T$ and $(.)^\dagger$ represent the transpose and pseudo-inverse, respectively. The symbols j, δ, $\mathbf{I}_m$, $\min\limits_x$ and $\|.\|_F^2$ denote the imaginary unit, Dirac delta function, $m\times m$ identity matrix, minimum value with decision variable x and Frobenius norm, respectively.

II. Fundamentals of Proposed Approach

A. Imaging System Model

Fig. 1 shows a general schematic of the multistatic imaging system in the proposed approach. The system includes n_T DMAs as Tx along the x-axis (horizontal) and a DMA along the y-axis (vertical) as the Rx. Each Tx and Rx DMA is a 1D aperture consisting of n_x and n_y sub-wavelength-sized metamaterial elements [29, 30] spaced at intervals d_x and d_y, respectively. It is assumed that the distance between the two adjacent Txs is d_T. By changing the operating frequency or voltage tuning, the radiation patterns from the Txs that illuminate the scene change. Voltage tuning here means the random *on*/*off* of each element by an external stimulus, which produces a set of masks [23, 31]. Each Tx DMA at any given frequency f can provide multiple measurements by cycling through M_T masks. Scene objects scatter the incident fields and generate a backscattered field that can be detected by Rx DMA (with M_R masks). The number of masks affects the overall diversity and complexity of the system.

Considering the use of DMA instead of independent dipoles in both Txs and Rx, the measurement signal [11] can be expressed as follows:

$$g_{l,m,m'}(f) \propto \int_V U_T^{[m]}(y_l,\vec{r};f)\,\rho(\vec{r})\,U_R^{[m']}(\vec{r};f)\,dV, \quad l=1,2,...,n_T, m=1,2,...,M_T, m'=1,2,...,M_R, \tag{1}$$

where $dV = dxdydz$, $y_l = y_1 + ld_T$ corresponds to the vertical position of the l-th Tx, ρ represents the reflectivity of the target, and $\vec{r}$ is the position vector to a point in the scene. In

the above equation, U_T and U_R are the radiated fields from the aperture, which can be expressed as the superposition of all metamaterial elements in each DMA as follows [24, 32]:

$$U_T^{[m]}(y_l,\vec{r};f) \propto \frac{Z_0 k\omega}{4\pi}\sum_{i=1}^{N}\frac{\vec{e}_i(f)}{|\vec{r}-x_i\hat{x}-y_l\hat{y}|}e^{-jk|\vec{r}-x_i\hat{x}-y_l\hat{y}|}\sin\theta,$$
$$U_R^{[m']}(\vec{r};f) \propto \frac{Z_0 k\omega}{4\pi}\sum_{i'=1}^{N}\frac{\vec{e}_{i'}(f)}{|\vec{r}-y_{i'}\hat{y}|}e^{-jk|\vec{r}-y_{i'}\hat{y}|}\sin\theta, \quad (2)$$

where $\omega = 2\pi f$, and Z_0 , $k=\omega/c$, c , θ , $\hat{x}$ and $\hat{y}$ denote the wave impedance in free space, wavenumber, the speed of light, the angle between $\vec{e}$ and $\vec{r}$, and the unit vector in the x - and y -directions, respectively. In the above equation, $\vec{e}_i(f)$ represents the relationship between each metamaterial element and the reference wave, which depends on the polarizability $\alpha_i(f)$. See [24, 32, 33] for more details.

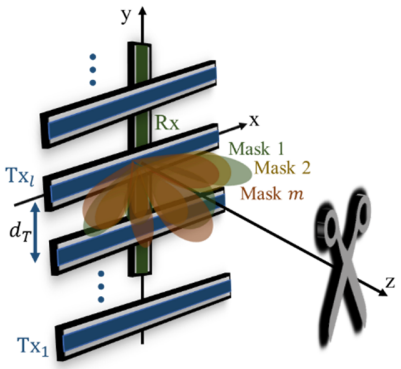

Fig. 1. General schematic of the multistatic imaging system in the proposed approach.

B. Image Reconstruction Algorithm

Assuming that the measured signal on the aperture plane can be expanded in terms of the fields associated with all the masks, we have

$$g_{l,m,m'}(f) = \sum_{i=1}^{n_x}\sum_{i'=1}^{n_y}\Phi_{T_{l,m}}(x_i;f)\,s_l(x_i,y_{i'};f)\,\Phi_{R_{m'}}(y_{i'};f), \quad (3)$$

where $s_l(x_i,y_{i'};f)$ denotes the incident field at the element's location corresponding to the l -th Tx, and x_i and $y_{i'}$ correspond to the positions of Tx and Rx. $\Phi_{T_{l,m}}$ and $\Phi_{R_{m'}}$ represent the field over the aperture corresponding to the m -th mask of the l -th Tx and the m' -th mask of Rx, respectively, and can be expressed as follows [23, 33, 34]:

$$\Phi_{T_{l,m}}(x_i;f) \propto Z_0 H_0 \alpha_{i,l,m}(f) e^{-j\beta(f)x_i},$$
$$\Phi_{R_{m'}}(y_{i'};f) \propto Z_0 H_0 \alpha_{i',m'}(f) e^{-j\beta(f)y_{i'}}, \quad (4)$$

where $i=1,2,...,n_x$ and $i'=1,2,...,n_y$. H_0 , $\beta = n_g\omega/c$ and n_g represent the guided magnetic field, the propagation constant of the waveguide and the waveguide index, respectively. The value of polarizability $\alpha(f)$ depends on the coupling factor (oscillator strength) F , resonance frequency ω_0 and damping factor $\gamma = \omega_0/(2Q)$, where Q is the quality factor of the metamaterial elements [33-35]. In fact, aperture fields mainly depend on the magnetic dipole moment induced in each element (for more details, refer to [34]). By assuming the creation of a set of aperture modes with some degrees of orthogonality, mathematically we have

$$\sum_{i=1}^{n_x}\Phi_{T_{l,m}}(x_i;f)\Phi^{\dagger}_{T_{l,\tilde{m}}}(x_i;f) \simeq \delta[m-\tilde{m}], \quad \tilde{m}\in[1,M_T],$$
$$\sum_{i'=1}^{n_y}\Phi^{\dagger}_{R_{\tilde{m}'}}(y_{i'};f)\Phi_{R_{m'}}(y_{i'};f) \simeq \delta[\tilde{m}'-m'], \quad \tilde{m}'\in[1,M_R]. \quad (5)$$

In practice, the method used in the dynamic metasurface aperture to generate a set of radiated fields with some degree of orthogonality is to employ different masks with random tuning states (random assignment of metamaterial elements throughout the array aperture). In (5), Φ_T and Φ_R represent the field distributions across the aperture of the metasurface realized by the random tuning states of the metasurface aperture, which are called "masks". If these masks exhibit some degree of orthogonality, then, (5) will apply. On a metasurface layer, such a dynamic modulation of the aperture can be achieved using metamaterial elements loaded with switch circuits, such as PIN diodes and varactors to name a few [36, 37]. Such a method (i.e. dynamic modulation of radiated fields) can be leveraged as an alternative to the frequency-diversity approach to generate a set of random sensor fields with spatial diversity [38]. In (5), the pseudo-inverse is needed to mitigate the effect of correlations, especially for magnitude compensation. The matched-filtering is a robust alternative to phase matching only [39, 40]. Coherent summation of frequency information in the final target estimation also helps to mitigate artifacts due to the correlation of aperture fields for different mask states.

According to (3), by multiplying $g_{l,m,m'}(f)$ by $\Phi^{\dagger}_{T_{l,\tilde{m}}}(x_{\tilde{i}};f)$ and $\Phi^{\dagger}_{R_{\tilde{m}'}}(y_{\tilde{i}'};f)$, where $\tilde{i}\in[1,n_x]$ and $\tilde{i}'\in[1,n_y]$, and then summing over the masks in the aperture domain

$$\sum_{m=1}^{M_T}\sum_{m'=1}^{M_R}\Phi^{\dagger}_{T_{l,\tilde{m}}}(x_{\tilde{i}};f)\,g_{l,m,m'}(f)\,\Phi^{\dagger}_{R_{\tilde{m}'}}(y_{\tilde{i}'};f) =$$
$$\sum_{m=1}^{M_T}\sum_{m'=1}^{M_R}\sum_{i=1}^{n_x}\sum_{i'=1}^{n_y}\Phi_{T_{l,m}}(x_i;f)\Phi^{\dagger}_{T_{l,\tilde{m}}}(x_{\tilde{i}};f)\,s_l(x_i,y_{i'};f)\times$$
$$\Phi^{\dagger}_{R_{\tilde{m}'}}(y_{\tilde{i}'};f)\Phi_{R_{m'}}(y_{i'};f). \quad (6)$$

For $i=\tilde{i}$ and $i'=\tilde{i}'$, and with respect to (5), (6) can be rewritten as follows:

$$\sum_{m=1}^{M_T}\sum_{m'=1}^{M_R}\Phi^{\dagger}_{T_{l,\tilde{m}}}\left(x_{\tilde{i}};f\right)g_{l,m,m'}\left(f\right)\Phi^{\dagger}_{R_{\tilde{m}'}}\left(y_{\tilde{i}'};f\right) \simeq \sum_{m=1}^{M_T}\sum_{m'=1}^{M_R}\delta\left[m-\tilde{m}\right]s_l\left(x_i,y_{i'};f\right)\delta\left[\tilde{m}'-m'\right], \tag{7}$$

Finally, using the delta function screening property, (7) can be simplified as follows:

$$s_l\left(x_i,y_{i'};f\right)\simeq\sum_{m=1}^{M_T}\sum_{m'=1}^{M_R}\Phi^{\dagger}_{T_{l,m}}\left(x_i;f\right)g_{l,m,m'}\left(f\right)\Phi^{\dagger}_{R_{m'}}\left(y_{i'};f\right). \tag{8}$$

Equation (8) states that by using a collection of measurements obtained by several dynamic metasurfaces (i.e. $g_{l,m,m'}\left(f\right)$), the field at the aperture plane can be estimated at points of equal spacing, which can be considered as effective dipole sources, (i.e. $s_l\left(x_i,y_{i'};f\right)$). Therefore, we now have data consistent with fast Fourier calculations. Equation (8) can be written in matrix form and as a function of frequency as follows:

$$\mathbf{s}_l\left(f\right)\simeq\mathbf{\Phi}^{\dagger}_{T_l}\left(f\right)\mathbf{g}_l\left(f\right)\mathbf{\Phi}'_R\left(f\right), \tag{9}$$

so that

$$\mathbf{\Phi}_{T_l}\left(f\right)\mathbf{\Phi}^{\dagger}_{T_l}\left(f\right)=\mathbf{I}_{M_T},\quad \mathbf{\Phi}'_R\left(f\right)\mathbf{\Phi}^{T}_{R}\left(f\right)=\mathbf{I}_{M_R}, \tag{10}$$

where $\mathbf{\Phi}'_R\left(f\right)\triangleq\left(\mathbf{\Phi}^{T}_R\left(f\right)\right)^{\dagger}$, $\mathbf{s}_l\left(f\right)\in\mathbb{C}^{n_x\times n_y}$, $\mathbf{\Phi}_{T_l}\left(f\right)\in\mathbb{C}^{M_T\times n_x}$, $\mathbf{\Phi}_R\left(f\right)\in\mathbb{C}^{M_R\times n_y}$ and $\mathbf{g}_l\left(f\right)\in\mathbb{C}^{M_T\times M_R}$. We have provided an analysis about the realization of (10) in Section III.

According to the geometry of the system in Fig. 1, the incident field $s\left(x_i,y_l,y_{i'};f\right)=s_l\left(x_i,y_{i'};f\right)$ can be written as follows:

$$s\left(x_i,y_l,y_{i'};f\right)=\int_V\frac{\rho\left(x,y,z\right)}{16\pi^2R_{T_l}R_R}e^{-jkR_{T_l}}e^{-jkR_R}dV, \tag{11}$$

where

$$R_{T_l}=\sqrt{\left(x-x_i\right)^2+\left(y-y_l\right)^2+z^2},\quad R_R=\sqrt{x^2+\left(y-y_{i'}\right)^2+z^2}. \tag{12}$$

By taking the 3D Fourier transform (FT) of both sides in (11) on the aperture coordinates, the representation of the signal s in the wavenumber domain can be expressed as

$$\begin{aligned}S\left(k_{xT},k_{yT},k_{yR},k\right)&\triangleq\mathrm{FT}_{3\mathrm{D}}\left\{s\left(x_i,y_l,y_{i'};f\right)\right\}=\\&\int_{A_T}\int_{y_{l'}}s\left(x_i,y_l,y_{i'};f\right)e^{-jk_{xT}x_i}e^{-jk_{yT}y_l}e^{-jk_{yR}y_{l'}}dy_{l'}dA_T\\&=\int_V\frac{\rho\left(x,y,z\right)}{16\pi^2}\underbrace{\int_{y_{l'}}\frac{e^{-jkR_R}}{R_R}e^{-jk_{yR}y_{l'}}dy_{l'}}_{\mathrm{I}_1}\times\\&\qquad\underbrace{\int_{A_T}\frac{e^{-jkR_T}}{R_T}e^{-jk_{xT}x_i}e^{-jk_{yT}y_l}dA_T}_{\mathrm{I}_2}dV,\end{aligned} \tag{13}$$

where $dA_T=dx_idy_l$. By expressing integrals I_1 and I_2 in particular oscillatory integral forms [41], respectively, in order to use the method of stationary phase for single and double integrals [42], and applying some mathematical operators, approximations and simplifications, the result can be written as follows:

$$\begin{aligned}\mathrm{I}_1&\simeq\left(1-j\right)\sqrt{\frac{\pi}{4k\sqrt{k^2-k_{yR}^2}}}e^{-jk_{yR}y}e^{-j\sqrt{k^2-k_{yR}^2}z},\quad k^2\geq k_{yR}^2,\\\mathrm{I}_2&\simeq\frac{-j2\pi}{\sqrt{k^2-k_{xT}^2-k_{yT}^2}}e^{-jk_{xT}x}e^{-jk_{yT}y}e^{-j\sqrt{k^2-k_{xT}^2-k_{yT}^2}z},\\&\qquad k^2\geq k_{xT}^2+k_{yT}^2.\end{aligned} \tag{14}$$

Details of the steps for calculating integrals such as I_1 and I_2 can be found in [34] and [43], respectively. These calculations mainly involve convolution theory, second-order 2D Taylor expansion, and first- and second-order partial derivatives. By substituting (14) in (13), the following simplified equation is obtained:

$$\begin{aligned}&S\left(k_{xT},k_{yT},k_{yR},k\right)\simeq\\&\int_V\frac{-\left(1+j\right)\rho\left(x,y,z\right)}{16\sqrt{\pi k}\left(k^2-k_{yR}^2\right)^{\frac{1}{4}}\sqrt{k^2-k_{xT}^2-k_{yT}^2}}e^{-jk_{xT}x}e^{-j\left(k_{yT}+k_{yR}\right)y}\times\\&\qquad e^{-j\sqrt{k^2-k_{xT}^2-k_{yT}^2}z}e^{-j\sqrt{k^2-k_{yR}^2}z}dV,\quad k^2\geq k_{yR}^2,k^2\geq k_{xT}^2+k_{yT}^2.\end{aligned} \tag{15}$$

The interpolated signal $\hat{S}$ can be written as follows:

$$\hat{S}\left(k_x,k_y,k_z\right)=\frac{-\left(1+j\right)}{16\sqrt{\pi k}\left(k^2-k_{yR}^2\right)^{\frac{1}{4}}\sqrt{k^2-k_x^2-k_{yT}^2}}\int_z\int_y\int_x\rho\left(x,y,z\right)e^{-jk_xx}e^{-jk_yy}e^{-jk_zz}dxdydz, \tag{16}$$

where

$$k_x = k_{xT}, k_y = k_{yT} + k_{yR}, k_z = \sqrt{k^2 - k_x^2 - k_{yT}^2} + \sqrt{k^2 - k_{yR}^2}, \quad k^2 \geq k_{yR}^2, k^2 \geq k_x^2 + k_{yT}^2. \tag{17}$$

Mapping $S\left(k_{xT}, k_{yT}, k_{yR}, k\right)$ to $\hat{S}\left(k_x, k_y, k_z\right)$ is performed by the Stolt interpolation operation [44] according to the dispersion relation in (17). From (16) it can be found that to recover the reflectivity $\rho(x, y, z)$, a filtering in the Fourier domain (corresponding to the term $-\pi\sqrt{\pi/k}\,(1+j)\left(k^2 - k_{xT}^2 - k_{yT}^2\right)^{-1/2}\left(k^2 - k_{yR}^2\right)^{-1/4}$) must be applied to $\hat{S}$ with a 3D inverse FT (IFT).

Remark 1: Note that in a conventional imaging system, when faced with a collection of independent antennas (point-like isotropic sources), considering the first Born approximation [45], the total field can be written mathematically in the following form:

$$s\left(x_i, y_l, y_{i'}; f\right) = \int_V G\left(x_i, y_l, \vec{r}; f\right)\rho\left(\vec{r}\right)G\left(y_{i'}, \vec{r}; f\right)dV, \tag{18}$$

where $G\left(\vec{r}', \vec{r}; f\right) = e^{-jk|\vec{r}-\vec{r}'|}\Big/\left(4\pi|\vec{r}-\vec{r}'|\right)$ represents Green's function [46] and $\vec{r}'$ is the dipole's location. However, the transceiver antennas considered in this paper (i.e. DMAs) cannot be modeled as individual dipoles. This is because the DMA concept relies on a physical layer compression [15, 47]. In other words, the scene information is sampled and encoded by the random transfer function of the DMA without the necessity to sample the aperture on a point-by-point (raster scan) basis. As a result, whereas reducing the number of channels to collect the backscattered data, in such a case, a more complex description of the signal is required for analysis, which is mathematically expressed in (1) and (2). It is clear that in (1), unlike (18), we do not have access to the field corresponding to $\vec{r}'$ (the fields corresponding to the positions x_i, y_i and $y_{i'}$). The pre-processing presented in this section is an effective way to transform the measurements provided by DMAs into a set equivalent to the spatial measurements emanating from a collection of effective dipole sources [34]. In fact, the operations after the presented pre-processing stage can be generalized and applied to the data collected from conventional antenna arrays.

C. CMS Scenario

According to the multiple-input single-output structure in Fig. 1, the above relationships are established when the receiver has access to the information corresponding to each Tx individually (individually measured signal (IMS) scenario). In fact, since we are dealing with multiple channels, we need to find a way to access the information of each channel. The simplest method is the time-division technique [48], in which only one Tx transmits at a time slot. However, this method may not be optimal for real-time applications. Coding-based methods can be an effective alternative [27, 28]. However, the advantage here is that in the previous section, we somehow encoded the aperture field, so we can use the same information to retrieve the data of each channel independently, without having to get involved in designing another coding mechanism.

Mathematically, CMS (the sum of the contributions of measurements for all Txs) can be written as follows:

$$\overline{g}_{m,m'}(f) \triangleq \sum_{l=1}^{n_T} g_{l,m,m'}(f). \tag{19}$$

The goal here is to get $s\left(x_i, y_l, y_{i'}; f\right)$ (or $\mathbf{s}_l(f)$) from signal $\overline{g}_{m,m'}(f)$ (or $\overline{\mathbf{g}}(f)$), in which case we will be able to apply the image reconstruction algorithm described in Section II-B to the CMS scenario as well. In the matrix form, by multiplying the left- and right-hand sides of $\mathbf{s}_l(f)$ in (9) by $\mathbf{\Phi}_{T_l}(f)$ and $\mathbf{\Phi}_R^T(f)$, respectively, considering (10) and expanding $\overline{\mathbf{g}}(f)$, we have

$$\overline{\mathbf{g}}(f) = \left(\sum_{l=1}^{n_T}\mathbf{\Phi}_{T_l}(f)\mathbf{s}_l(f)\right)\mathbf{\Phi}_R^T(f). \tag{20}$$

By multiplying the left- and right-hand sides of $\overline{\mathbf{g}}(f) \in \mathbb{C}^{M_T \times M_R}$ in (20) by $\mathbf{\Phi}_{T_{l'}}^{\dagger}(f)$ and $\mathbf{\Phi}_R'(f)$, respectively, where $l' = 1, 2, ..., n_T$, and naming the result as $\tilde{\mathbf{s}}_{l'}(f)$, we have

$$\begin{aligned}\tilde{\mathbf{s}}_{l'}(f) &\triangleq \mathbf{\Phi}_{T_{l'}}^{\dagger}(f)\overline{\mathbf{g}}(f)\mathbf{\Phi}_R'(f)\\ &= \mathbf{\Phi}_{T_{l'}}^{\dagger}(f)\left(\sum_{l=1}^{n_T}\mathbf{\Phi}_{T_l}(f)\mathbf{s}_l(f)\right)\mathbf{\Phi}_R^T(f)\mathbf{\Phi}_R'(f)\\ &= \mathbf{\Phi}_{T_{l'}}^{\dagger}(f)\mathbf{\Phi}_{T_1}(f)\mathbf{s}_1(f)\mathbf{\Phi}_R^T(f)\mathbf{\Phi}_R'(f)\\ &+ \mathbf{\Phi}_{T_{l'}}^{\dagger}(f)\mathbf{\Phi}_{T_2}(f)\mathbf{s}_2(f)\mathbf{\Phi}_R^T(f)\mathbf{\Phi}_R'(f) + ...\\ &+ \mathbf{\Phi}_{T_{l'}}^{\dagger}(f)\mathbf{\Phi}_{T_{n_T}}(f)\mathbf{s}_{n_T}(f)\mathbf{\Phi}_R^T(f)\mathbf{\Phi}_R'(f).\end{aligned} \tag{21}$$

By calculating $\tilde{\mathbf{s}}_{l'}(f)$ for all l's, we will have n_T matrix equations that can be written as a system of equations in block matrix form (as presented in (22)), and its equivalent is given in (23)

$$\underbrace{\begin{bmatrix}\tilde{\mathbf{s}}_1(f)\\ \tilde{\mathbf{s}}_2(f)\\ \vdots\\ \tilde{\mathbf{s}}_{n_T}(f)\end{bmatrix}}_{\mathbf{G}_{n_T n_x\times n_y}(f)}= \underbrace{\begin{bmatrix}\boldsymbol{\Theta}_{1,1}(f) & \boldsymbol{\Theta}_{1,2}(f) & \cdots & \boldsymbol{\Theta}_{1,n_T}(f)\\ \boldsymbol{\Theta}_{2,1}(f) & \boldsymbol{\Theta}_{2,2}(f) & \cdots & \boldsymbol{\Theta}_{2,n_T}(f)\\ \vdots & \vdots & \ddots & \vdots\\ \boldsymbol{\Theta}_{n_T,1}(f) & \boldsymbol{\Theta}_{n_T,2}(f) & \cdots & \boldsymbol{\Theta}_{n_T,n_T}(f)\end{bmatrix}}_{\boldsymbol{\Pi}_{n_T n_x\times n_T n_x}(f)} \underbrace{\begin{bmatrix}\boldsymbol{\Omega}_1(f)\\ \boldsymbol{\Omega}_2(f)\\ \vdots\\ \boldsymbol{\Omega}_{n_T}(f)\end{bmatrix}}_{\boldsymbol{\Psi}_{n_T n_x\times n_y}(f)}, \tag{23}$$

where $\boldsymbol{\Theta}_{l',l}(f)\triangleq\boldsymbol{\Phi}_{T_{l'}}^{\dagger}(f)\boldsymbol{\Phi}_{T_l}(f)$, $\boldsymbol{\Omega}_l(f)\triangleq\mathbf{s}_l(f)\boldsymbol{\beta}(f)$ and $\boldsymbol{\beta}(f)\triangleq\boldsymbol{\Phi}_R^T(f)\boldsymbol{\Phi}_R'(f)$. The unknown of the above system of equations (i.e. $\boldsymbol{\Sigma}_{n_T n_x\times n_y}(f)\triangleq\left[\mathbf{s}_1(f),\mathbf{s}_2(f),...,\mathbf{s}_{n_T}(f)\right]^T$) is retrieved as follows:

$$\boldsymbol{\Sigma}(f)=\boldsymbol{\Psi}(f)\boldsymbol{\beta}^{\dagger}(f), \tag{24}$$

where block matrix $\boldsymbol{\Psi}(f)$ can be computed by solving the following least-squares problem (see (23)):

$$\min_{\boldsymbol{\Psi}(f)}\left\|\boldsymbol{\Pi}(f)\boldsymbol{\Psi}(f)-\mathbf{G}(f)\right\|_F^2. \tag{25}$$

Remark 2: According to (4), since the value of $\boldsymbol{\Phi}_{T_l}(f)$ is dependent on i (index of elements) and x_i, therefore, regardless of the state of the masks, $\boldsymbol{\Phi}_{T_l}(f)$ must be a full column rank matrix; so $\boldsymbol{\Theta}_{l,l}(f)=\mathbf{I}_{n_x}$. As a result, the rank of $\boldsymbol{\Pi}(f)$ is at least equal to n_x. Therefore, $\boldsymbol{\Pi}(f)$ is not necessarily invertible and the calculation of $\boldsymbol{\Psi}(f)$ using a generalized inverse does not lead to a unique solution. For this reason, in (25) we use a minimum norm least-squares technique [49, 50], which minimizes the norm of $\boldsymbol{\Psi}(f)$ in addition to minimizing the norm of $\boldsymbol{\Pi}(f)\boldsymbol{\Psi}(f)-\mathbf{G}(f)$. In this technique, complete orthogonal decomposition is used to find a low-rank approximation of $\boldsymbol{\Pi}(f)$. For more details, refer to [49, 50].

Note that $\boldsymbol{\Pi}^{\dagger}$ and $\boldsymbol{\beta}$ can be calculated once and stored in memory, so they are not part of the online calculations in processing. It is also worth emphasizing that one dimension of the raw data corresponds to the frequency samples; therefore, all the above matrix calculations are done independently for each frequency sample.

III. Simulation Results and Discussion

In this section, to examine the performance of the proposed approach, the results of numerical simulations in MATLAB are presented. All computations are performed in MATLAB R2020b running on a 64-bit Windows 11 operating system with 16 GB of random-access memory and a Core-i7 central processing unit at 2.8 GHz. The data of the numerical examples are simulated with the model presented in (1) and (2) under the Born approximation [51]. The values of the simulation parameters are given in Table I, where λ is the wavelength corresponding to the highest frequency in free space, n_f represents the number of frequency samples, z_0 is the target range, and D_z is the length of target space in the range direction. According to the Nyquist theorem, the frequency sampling step must satisfy the condition $\Delta_f\le c/(2D_z)$ [52]. According to the values of D_z, bandwidth and number of frequency samples presented in Table I, the Nyquist condition is satisfied in the simulations. Also, according to the values in Table I, the theoretical resolutions of cross-range and range [11] are approximately equal to 1.07 cm and 3.33 cm respectively.

Before image reconstruction, let us check the condition of (10), i.e., having a set of aperture modes with some degrees of orthogonality. For this purpose, as an instance, we extract the singular values (SVs) of $\boldsymbol{\Phi}_{T_1}(f)$, denoted by $\sigma_1\ge\sigma_2\ge...\ge\sigma_P\in\mathbb{R}^+$, where $P=\min(n_x,M_T)$. In general, the corresponding SVs matrix is quasi-diagonal so that the SVs are arranged from largest to smallest on its main diagonal. If

---

$$\begin{bmatrix}\tilde{\mathbf{s}}_1(f)\\ \tilde{\mathbf{s}}_2(f)\\ \vdots\\ \tilde{\mathbf{s}}_{n_T}(f)\end{bmatrix}=\begin{bmatrix}\boldsymbol{\Phi}_{T_1}^{\dagger}(f)\boldsymbol{\Phi}_{T_1}(f) & \boldsymbol{\Phi}_{T_1}^{\dagger}(f)\boldsymbol{\Phi}_{T_2}(f) & \cdots & \boldsymbol{\Phi}_{T_1}^{\dagger}(f)\boldsymbol{\Phi}_{T_{n_T}}(f)\\ \boldsymbol{\Phi}_{T_2}^{\dagger}(f)\boldsymbol{\Phi}_{T_1}(f) & \boldsymbol{\Phi}_{T_2}^{\dagger}(f)\boldsymbol{\Phi}_{T_2}(f) & \cdots & \boldsymbol{\Phi}_{T_2}^{\dagger}(f)\boldsymbol{\Phi}_{T_{n_T}}(f)\\ \vdots & \vdots & \ddots & \vdots\\ \boldsymbol{\Phi}_{T_{n_T}}^{\dagger}(f)\boldsymbol{\Phi}_{T_1}(f) & \boldsymbol{\Phi}_{T_{n_T}}^{\dagger}(f)\boldsymbol{\Phi}_{T_2}(f) & \cdots & \boldsymbol{\Phi}_{T_{n_T}}^{\dagger}(f)\boldsymbol{\Phi}_{T_{n_T}}(f)\end{bmatrix}\begin{bmatrix}\mathbf{s}_1(f)\boldsymbol{\Phi}_R^T(f)\boldsymbol{\Phi}_R'(f)\\ \mathbf{s}_2(f)\boldsymbol{\Phi}_R^T(f)\boldsymbol{\Phi}_R'(f)\\ \vdots\\ \mathbf{s}_{n_T}(f)\boldsymbol{\Phi}_R^T(f)\boldsymbol{\Phi}_R'(f)\end{bmatrix}. \tag{22}$$

TABLE I
VALUES OF SIMULATION PARAMETERS

Parameter	$N_x=N_y$	$d_x=d_y$	N_T	d_T	f	n_f	$M_T=M_R$	Q	Z_0	n_g	F	z_0	D_z
Value	105	6.81 mm ($\lambda/2$)	3	354.3 mm (26λ)	17.5-22 GHz	51	105	50	120π	2.5	1	0.5 m	0.5 m

$\mathbf{\Phi}_{T_1}^{H}(f)\mathbf{\Phi}_{T_1}(f)$ is invertible (in other words, $\text{rank}\left(\mathbf{\Phi}_{T_1}(f)\right)$ is P), then $1/\sigma_P \geq 1/\sigma_{P-1} \geq \ldots \geq 1/\sigma_1$ will be the SVs of $\mathbf{\Phi}_{T_1}^{\dagger}(f)$. The closer the SVs of the aperture field matrix are to each other, the more equally the singular vectors are weighted in signal reconstruction. In other words, masks become more independent. Fig. 2(a) shows the aperture field matrix $\mathbf{\Phi}_{T_1}$ at 22 GHz in the case created by a set of masks with only one unique element *on* in each mask (here called the *identity* case). Fig. 3 shows the spectrum of the corresponding SVs. Also, the ratio of the largest SV to the smallest, which is called the condition number r, has been calculated. As can be seen, the corresponding diagram has a very small slope. The value r also confirm this. According to the above explanation, this indicates that the *identity* case is very favorable in terms of orthogonality required for the aperture field matrix. However, it results in very little radiated power. Therefore, in practice, more elements need to be turned on. Fig. 2(c) shows a case (called *random*) in which half of the elements in each mask are randomly turned on. In this case, more energy is radiated to the scene, which leads to a more robust system against the noise. This comes at the cost of relative correlation between the radiation patterns, the effect of which can be seen in Fig. 3 as a steeper slope of the corresponding diagram as well as an increase in the value of r. Also, by comparing the largest SVs, it can be concluded that the *random* case has more radiated power than the *identity* case. Fig. 4 shows a representation of $\mathbf{\Phi}_{T_1}\mathbf{\Phi}_{T_1}^{\dagger}$ in different cases at 22 GHz. It can be seen that although the second case is not perfect in terms of orthogonality compared to the identity case, the condition of (10) is still fulfilled. In other words, both above can be used for the pre-processing step. However, this degree of freedom is not unlimited. Fig. 2(c) shows the case in which 99% of the elements (almost all of them) are *on* (here it is called the *full* case). As shown in Fig. 3, the corresponding diagram experiences a steep slope in the areas related to large SVs. In addition, after the 64th SV, there is a sharp drop towards very small values. This means that the aperture field matrix has a rank equal to 64 (it has suffered a rank loss); while in both *identity* and *random* cases, the aperture field matrix is of full rank ($\text{rank}\left(\mathbf{\Phi}_{T_1}\right)=105$). It can also be seen that the value of r in the third case is almost infinite. Note that in Fig. 3, for a clearer comparison, only a part of the green diagram is shown. What can be concluded is that only the third case does not satisfy condition of (10) (see Fig. 4) and is not suitable for use in the proposed pre-processing step. Note that similar analyzes can be performed for other aperture field matrices corresponding to other Tx and Rx DMAs. To further study, we extended the results presented in Fig. 3; in this way, we calculated the average value of r in 1000 independent experiments for the different number of masks and different percentages of *on* elements (denoted by P). The relevant results are shown in Fig. 5. It can be seen that, in general, as P increases, the value of r increases; in other words, the lower the percentage of *on* elements, the more reliable conditions are provided in terms of orthogonality. On the other hand, as mentioned in the discussions related to Fig. 3, a low percentage of the number of *on* elements means low radiated power (hence a low signal-to-noise ratio). Therefore, considering a moderate value for P (in this case half of the elements *off*) can provide a reasonable compromise between both orthogonality and robustness against noise. By considering the efficient features of the *random* case mentioned above, the results presented in the rest of this paper are obtained based on it.

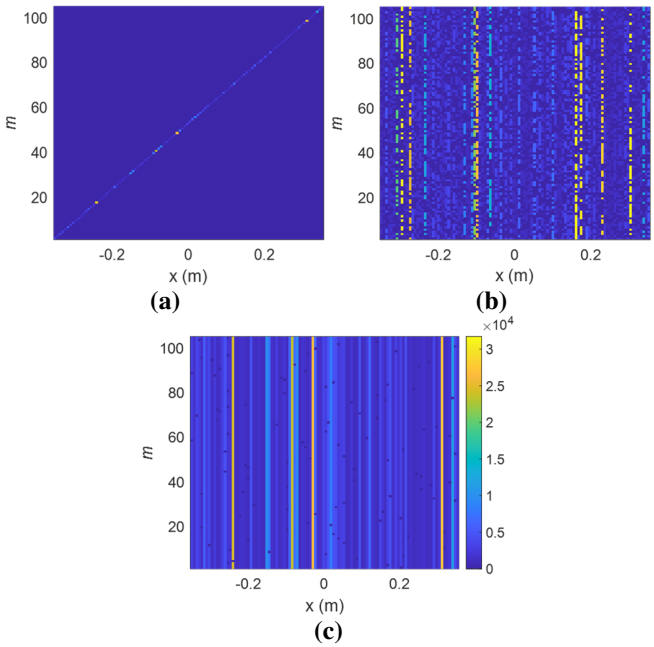

Fig. 2. $\mathbf{\Phi}_{T_1}$ at 22 GHz; **(a)** in *identity* case, **(b)** in *random* case, **(c)** in *full* case.

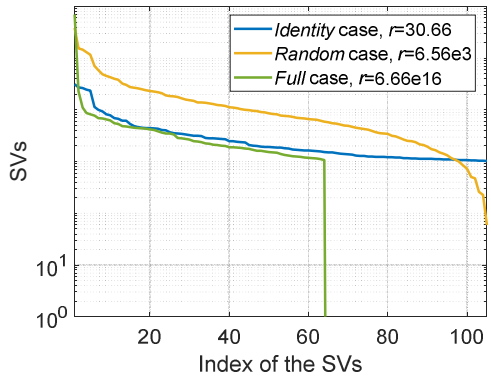

Fig. 3. SVs spectra and condition numbers corresponding to the outputs of Fig. 2.

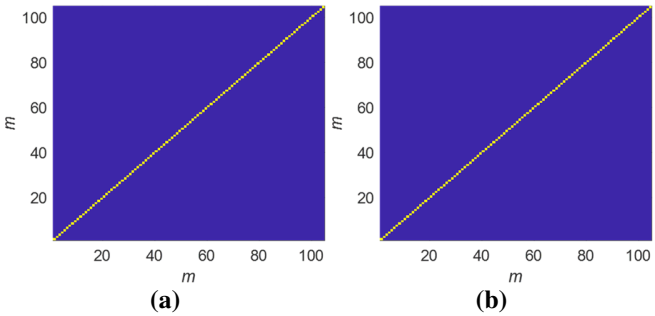

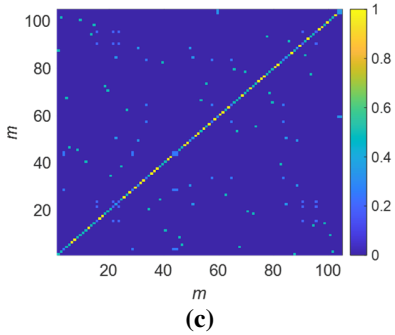

(c)

Fig. 4. Checking the realization of (10) in the case of the aperture field matrix $\mathbf{\Phi}_{T_1}$ for the outputs of Fig. 2; **(a)** $\mathbf{\Phi}_{T_1}\mathbf{\Phi}_{T_1}^{\dagger}$ in *identity* case, **(b)** $\mathbf{\Phi}_{T_1}\mathbf{\Phi}_{T_1}^{\dagger}$ in *random* case, **(c)** $\mathbf{\Phi}_{T_1}\mathbf{\Phi}_{T_1}^{\dagger}$ in *full* case.

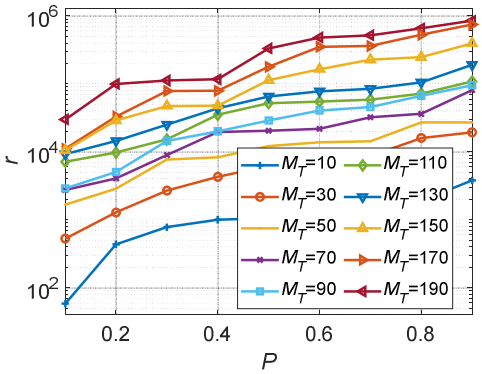

Fig. 5. Average value of r in 1000 independent experiments for the different number of masks and different percentages of *on* elements.

In the next experiment, we consider five point scatterers located at $(-0.1, 0.08, z_0 - 0.1)$, $(-0.05, 0.04, z_0 - 0.05)$, $(0, 0, z_0)$, $(0.05, -0.04, z_0 + 0.05)$ and $(0.1, -0.08, z_0 + 0.1)$, all in meters, as targets. The reconstructed images in IMS and CMS cases after applying all the processing steps are shown in Figs. 6(a) and 6(b) respectively (in different 2D and 3D views). As can be seen in both cases, the proposed approach has been able to successfully reconstruct the image of all point scatterers in their correct positions. The reason that the detected points become smaller with increasing distance from the radar is the propagation loss effect, which is consistent with the analyzes and findings presented in [34, 53].

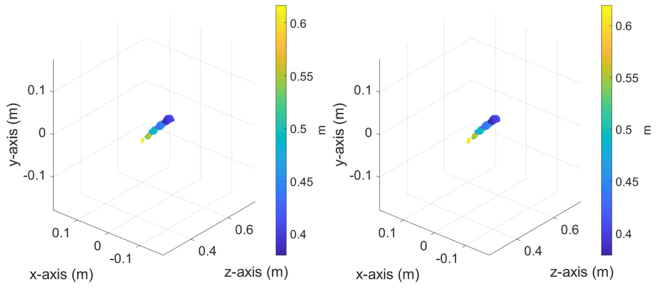

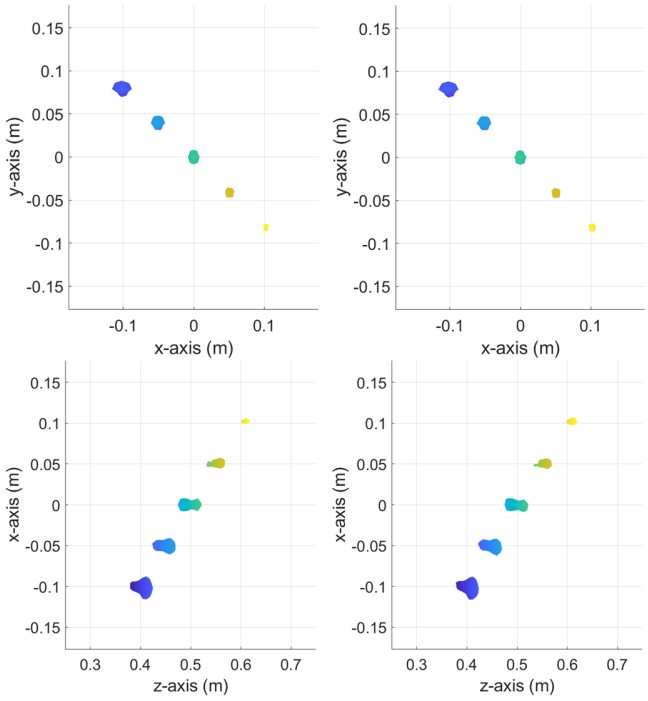

(a) **(b)**

Fig. 6. Reconstructed images of five point scatterers by the proposed approach in different 3D and 2D views; (a) in the IMS scenario, (b) in the CMS scenario. Isovalue: -10 dB.

Now let us compare the performance of the image reconstruction algorithms. A scissor (see Fig. 1) is under test as a 3D distributed target in the near-field [54, 55]. Fig. 7 shows the reconstructed images by approaches [5, 6], [11, 23] and [21], and the proposed approach in 3D and 2D views. Visually, it can be seen that Fig. 7(d) (output of the proposed approach in the IMS scenario), in both views, provides the lowest level of sidelobe and distortion compared to the other figures. Although Fig. 7(c) (output of approach [21]) shows good quality in 2D view (x-y), in 3D view it is clear that it does not have a good range resolution compared to the output of other approaches. The reason for this is to use the nonuniform inverse fast Fourier transform (NUIFFT) + 2D IFFT operation instead of the Stolt interpolation + 3D IFFT operation in the image reconstruction algorithm. Although it reduces computational complexity, it provides lower quality [21]. Fig. 7(f) shows that in the CMS scenario, when the proposed pre-processing technique is not applied to the raw measured data, the reconstructed image is meaningless (with no indication of the target). The reason for this is obvious because the raw signal measured in this scenario is superposition of data from all Txs, and the processing algorithm lacks access to the information of each channel separately. However, when the proposed pre-processing (presented in Section II-C) is applied to the raw data, the reconstructed image correctly reveals the target information (see Fig. 7(e)). Clearly, in this case, the output cannot be expected to have the quality obtained in the IMS scenario; because in practice the orthogonalities between the field matrices are not perfect. Note that in the case of Fig. 7(a), the results were obtained based on using conventional linear arrays with independent antennas (and with an aperture size equivalent

to those other results), and employing the generalized synthetic aperture focusing technique (GSAFT) [5, 6] to reconstruct the image. The number of voxels considered in this case to render the scene is equal to $N_x' \times N_y' \times N_z' = 53 \times 53 \times 53$.

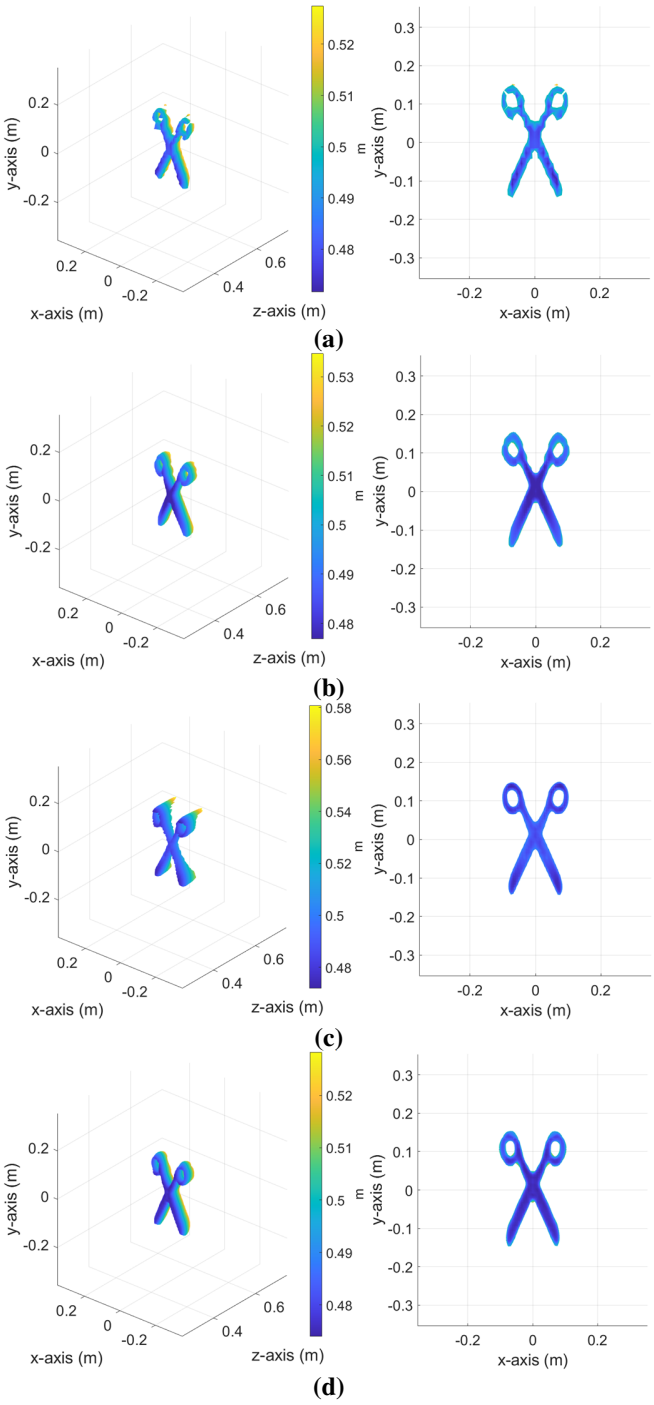

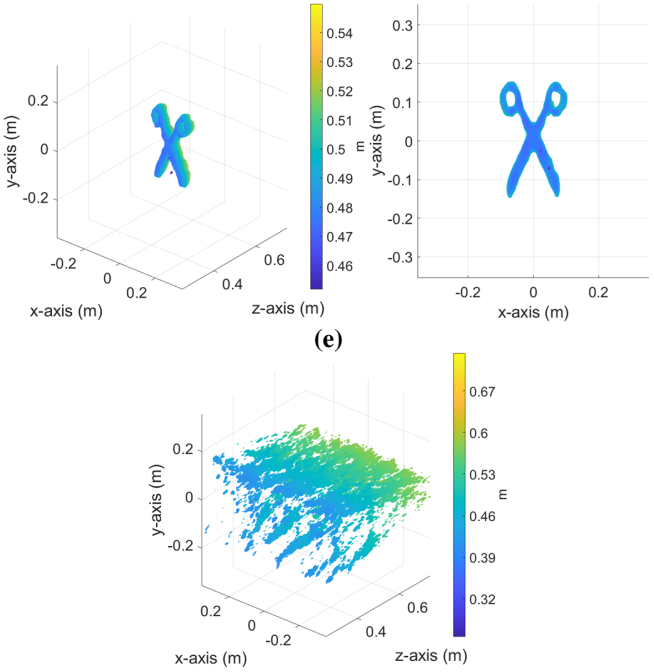

Fig. 7. Images reconstructed by different methods in 3D and 2D views; **(a)** GSAFT [5, 6], **(b)** approach [11, 23], **(c)** approach [21], **(d)** proposed approach (IMS), **(e)** proposed approach (CMS), **(f)** CMS without proposed pre-processing. Isovalue: -10 dB.

We also evaluated the quality of the reconstructed images with quantitative measures (normalized mean squared error (NMSE) [56], image contrast (IC) [57] and image entropy (IE) [57]:

$$\mathrm{NMSE} = \frac{\sum_{i=1}^{N_x'}\sum_{i'=1}^{N_y'}\sum_{i''}^{N_z'}\left|\rho_{\mathrm{Rec}}\left(x_i, y_{i'}, z_{i''}\right) - \rho_{\mathrm{Ref}}\left(x_i, y_{i'}, z_{i''}\right)\right|^2}{\sum_{i=1}^{N_x'}\sum_{i'=1}^{N_y'}\sum_{i''}^{N_z'}\left|\rho_{\mathrm{Ref}}\left(x_i, y_{i'}\right)\right|^2}, \quad (26)$$

$$\mathrm{IC}(I) = I_{\max} - I_{\min}, \quad (27)$$

$$\mathrm{IE}(I) = -\sum_{k=0}^{L-1} p(k)\log_2 p(k), \quad (28)$$

where ρ_{Rec}, ρ_{Ref}, $I_{\max}$, $I_{\min}$, $p(k)$ and $L = 2^q$ denote the reconstructed image, reference image, maximum value intensity, minimum value intensity, the probability of occurrence of the value k in the image I and the number of different gray levels. The results are given in Table II. Contrast and entropy values are calculated based on values averaged from 2D reconstructed images (on the xy-plane) focused on different ranges (when the pixel values are normalized by $q = 8$). For the NMSE measure, two metrics NMSE 1 and NMSE 2 have been calculated, respectively, when Fig. 7(b) and Fig. 7(d) are used as reference images. The results in Table II are consistent with the visual findings described in the previous

paragraph. By comparing the proposed approach in the CMS scenario with the approach [21], it can be seen that although the approach [21] has better contrast and entropy, the NMSE value is still higher. The reason for this is the low range resolution in the approach [21], which was also mentioned in the previous paragraph.

In addition to comparing the quality of the reconstructed images, we calculated the major complexities involved in the implementation steps of the algorithms in the various approaches, as well as the corresponding computational times. These steps in the case of Fourier-based algorithms include a pre-processing operation to convert the raw measured data to the spatial-frequency domain, FFT, IFFT, NUIFFT and Stolt interpolation. In the case of GSAFT, the calculations lack the above steps (it has a Fourier calculation-free scheme). Its complexity is mainly involved in excessive computations of received signal phase compensation based on the calculation of vectors between the position of each pair of Tx and Rx antennas and each voxel of the target by discretizing the target space into multiple voxels. The number of these voxels has a decisive role in the computational time and the quality of the image in the GSAFT outputs. The computational times are given separately in Table III. As can be seen and expected, in the case of Fourier-based approaches, most of the computational load is related to the Stolt interpolation stage. The longer computational time of this step in the proposed approach than the approach [11, 23] is due to an increase in the interpolation dimensions. In the approach [11, 23], a 3D to 3D interpolation is required, while in the proposed approach, a 4D to 3D interpolation is needed. However, the proposed approach takes advantage of panel-to-panel configuration without the need for mechanical scanning as well as improved reconstructed image quality. Although processing time can provide an initial idea of computational efficiency, computational complexity provides a more reliable picture. In Table IV the computational complexities are listed by steps in different approaches. N_y, n_p, n_i, M_s and M_r, respectively, represent the number of point source sampling points along the y-axis, padded signal length, order of the multiplicative complexity for one Stolt's mapping [58], spreading parameter [21, 59] and oversampling number [21, 59]. Based on the information in Table IV, Figs. 8(a) and 8(b) show the total computational complexity of the different approaches versus the number of frequency samples and the number of DMA elements, respectively. It is clear that as the number of samples/elements increases, so does the complexity. As expected, the computational complexity of the proposed approach is greater than that of the approaches [11, 23] and [21]. The main reason is related to the Stolt interpolation stage, which, in a multistatic structure, contributes to the overall diversity of the system, whereas inevitably increasing the interpolation dimensions. In any case, the proposed approach

TABLE II
COMPARISON OF NMSE, IMAGE CONTRAST AND IMAGE ENTROPY VALUES CALCULATED IN DIFFERENT METHODS

Approach	NMSE 1	NMSE 2	Contrast	Entropy
GSAFT [5, 6]	2.28	1.17	98.68	5.61
[11, 23]	Reference image	0.55	136.74	6.25
[21]	2.29	1.08	117.52	6.19
Proposed (IMS)	0.44	Reference image	163.97	6.36
Proposed (CMS)	0.75	0.65	105.3	5.77
CMS without proposed pre-processing	15.82	21.49	96.48	5.58

TABLE III
COMPARISON OF AVERAGE COMPUTATIONAL TIMES FOR PERFORMING MAJOR COMPUTATIONAL STEPS (SEC)

Operation / Approach	Pre-processing	FFT	Stolt Interpolation	NUIFFT	IFFT	Total
[11, 23]	0.64	0.022	2.44	-	0.058	3.16
[21]	0.64	0.022	-	1.14	0.0078	1.81
Proposed (IMS)	1.56	0.64	11.07	-	0.058	13.33
Proposed (CMS)	3.97	0.64	11.07	-	0.058	15.74
GSAFT [5, 6]	Compensation of the received signal phase					888.75

TABLE IV
COMPARISON OF MAJOR COMPUTATIONAL COMPLEXITIES

Operation / Approach	Pre-processing	FFT	Stolt Interpolation	NUIFFT	IFFT
[11, 23]	$\mathcal{O}\left(n_f N_y n_x M_T\right)$	$\mathcal{O}\left(n_f n_x N_y \log_2\left(n_x N_y\right)\right)$	$\mathcal{O}\left(n_x N_y n_i\right)$	-	$\mathcal{O}\left(n_x N_y n_z \log_2\left(n_x N_y n_z\right)\right)$
[21]	$\mathcal{O}\left(n_f N_y n_x M_T\right)$	$\mathcal{O}\left(n_f n_x N_y \log_2\left(n_x N_y\right)\right)$	-	$\mathcal{O}\left(n_x N_y \left(M_s n_f + 0.5 M_r log M_r\right)\right)$	$\mathcal{O}\left(n_x N_y \log_2\left(n_x N_y\right)\right)$
Proposed (IMS)	$\mathcal{O}\left(n_T n_f n_x M_R \left(M_T + n_y\right)\right)$	$\mathcal{O}\left(n_f n_x n_y n_p \log_2\left(n_x n_y n_p\right)\right)$	$\mathcal{O}\left(n_x n_y n_p n_i\right)$	-	$\mathcal{O}\left(n_x n_p n_z \log_2\left(n_x n_p n_z\right)\right)$
Proposed (CMS)	$\mathcal{O}\left(n_T n_f n_x \left(M_R M_T + M_R n_y + n_T n_x n_y + n_y n_y\right)\right)$	$\mathcal{O}\left(n_f n_x n_y n_p \log_2\left(n_x n_y n_p\right)\right)$	$\mathcal{O}\left(n_x n_y n_p n_i\right)$	-	$\mathcal{O}\left(n_x n_p n_z \log_2\left(n_x n_p n_z\right)\right)$
GSAFT	$\mathcal{O}\left(n_T n_f n_x n_y N'_x N'_y N'_z\right)$				

still has the significant advantage of fast Fourier computations compared to GSAFT [5, 6].

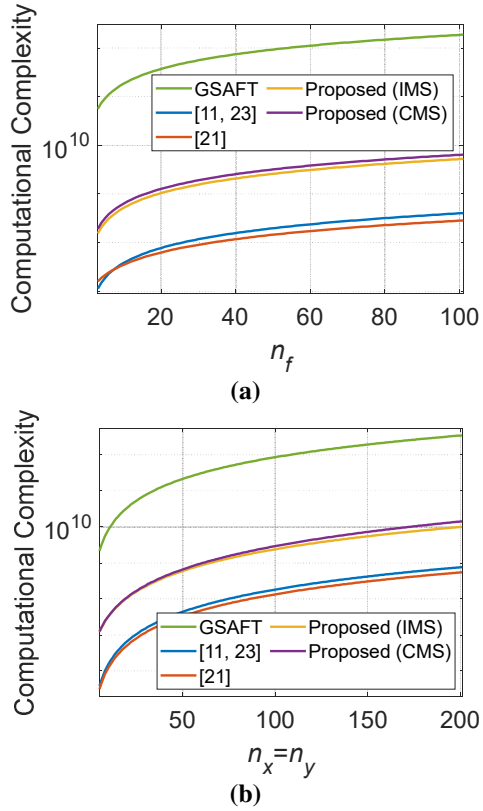

Fig. 8. The total computational complexity of different approaches; **(a)** versus the number of frequency samples, **(b)** versus the number of DMA elements.

IV. Conclusion and Future Works

In this paper, a panel-to-panel model with DMAs based on a multistatic structure is introduced; then two pre-processing were provided to convert the raw measurements collected by the above model to the spatial-frequency domain (for both IMS and CMS scenarios); finally, according to the introduced imaging system and the output data from the pre-processing stage, the RMA algorithm was developed to reconstruct a 3D image of the scene based on fast Fourier calculations. The idea and capability of using DMA diversity to achieve simultaneous data acquisition presented in this paper add a new purpose to the DMA concept in addition to diverse DMA modes for computational imaging. The performance of the proposed approach was evaluated in terms of the visual quality of the reconstructed image and computational complexity, and compared with state-of-art works. A summary of key features (including imaging configuration, aperture layout, scanning type, reconstructed image quality by NMSE measure (average NMSE values in Table II), and computational time) of the proposed approach compared to other works is given in Table V.

Although the proposed approach has more computational complexity compared to other Fourier-based approaches, in addition to eliminating mechanical scanning and improving the data acquisition mechanism, it provides better visual quality of the reconstructed image. Moreover, it still has the significant advantage of fast Fourier calculations and is much more efficient compared to conventional techniques such as GSAFT. The development of a proposed approach for multiple-input single-output (MIMO) and massive MIMO structures, as well as the improvement of the computational cost of the Stolt interpolation process, will be studied in future work.

In this paper, DMA aperture simulations were performed based on the mathematical models developed in the literature, whose main formulas, details, and references were mentioned in Section II-A and the beginning of Section II-B. Naturally, in the simulations performed in MATLAB, it cannot be expected that all the physical properties of materials will be taken into account in the same way as a full-wave simulator. However, our focus in this paper was on the processing layer with the specific goal of developing an image reconstruction algorithm based on fast Fourier calculations compatible with data collected in two practical scenarios of multistatic imaging using DMAs. For future works, the proposed approach will be studied, evaluated, analyzed and discussed with experimental data.

References

[1] H. Wu and R. K. Amineh, "A low-cost and compact three-dimensional microwave holographic imaging system," *Electronics,* vol. 8, no. 9, p. 1036, 2019.

TABLE V
A Summary of the Key Features of the Proposed Approach (in Two Different Scenarios) Compared to GSAFT [5, 6] and Approaches [11, 23] and [21]

Feature / Approach	Imaging Configuration	Aperture Layout	Scanning Type	Ability to Transmit Simultaneously	NMSE	Computational Time (Sec)
GSAFT [5, 6]	Magnetic dipoles (no DMA)	1D uniform array	Mixed electronically and mechanically	No	1.73	888.75
[11, 23]	Panel-to-probe	Tx DMA + waveguide probe	Mixed electronically and mechanically	No	0.55	3.16
[21]	Panel-to-probe	Tx DMA + waveguide probe	Mixed electronically and mechanically	No	1.69	1.81
Proposed (IMS)	Panel-to-panel	Multistatic DMA transceiver	Pure electronically	No	0.44	13.33
Proposed (CMS)	Panel-to-panel	Multistatic DMA transceiver	Pure electronically	Yes	0.7	15.74

[2] R. K. Amineh, N. K. Nikolova, and M. Ravan, *Real-Time Three-Dimensional Imaging of Dielectric Bodies Using Microwave/Millimeter Wave Holography*. John Wiley & Sons, 2019.
[3] L. Li *et al.*, "Intelligent metasurface imager and recognizer," *Light: science & applications,* vol. 8, no. 1, pp. 1-9, 2019.
[4] A. Raveendran and S. Raman, "Metamaterial-FSS Antenna for Microwave Image Sensing," in *Handbook of Metamaterial-Derived Frequency Selective Surfaces*: Springer, 2022, pp. 1-35.
[5] S. Hu, C. Shu, Y. Alfadhl, and X. Chen, "A THz imaging system using linear sparse periodic array," *IEEE Sensors Journal,* vol. 20, no. 6, pp. 3285-3292, 2019.
[6] A. M. Molaei, S. Hu, V. Skouroliakou, V. Fusco, X. Chen, and O. Yurduseven, "Fourier compatible near-field multiple-input multiple-output terahertz imaging with sparse non-uniform apertures," *IEEE Access,* vol. 9, pp. 157278-157294, 2021.
[7] M. Faenzi *et al.*, "Metasurface antennas: New models, applications and realizations," *Sci Rep,* vol. 9, no. 1, pp. 1-14, 2019.
[8] M. F. Imani *et al.*, "Review of metasurface antennas for computational microwave imaging," *IEEE transactions on antennas and propagation,* vol. 68, no. 3, pp. 1860-1875, 2020.
[9] L. Li, H. Zhao, C. Liu, L. Li, and T. J. Cui, "Intelligent metasurfaces: control, communication and computing," *eLight,* vol. 2, no. 1, pp. 1-24, 2022.
[10] M. F. Imani, T. Sleasman, J. N. Gollub, and D. R. Smith, "Analytical modeling of printed metasurface cavities for computational imaging," *Journal of Applied Physics,* vol. 120, no. 14, p. 144903, 2016.
[11] L. M. P. Mancera, "Analytical Modeling of Waveguide-fed Metasurfaces for Microwave Imaging and Beamforming," Duke University, 2018.
[12] G. Lan *et al.*, "MetaSense: Boosting RF Sensing Accuracy Using Dynamic Metasurface Antenna," *IEEE Internet of Things Journal,* vol. 8, no. 18, pp. 14110-14126, 2021.
[13] A. Pedross-Engel *et al.*, "Orthogonal coded active illumination for millimeter wave, massive-MIMO computational imaging with metasurface antennas," *IEEE Transactions on Computational Imaging,* vol. 4, no. 2, pp. 184-193, 2018.
[14] Z. Peixia, L. Yichen, and L. Hongchao, "Single-pixel imaging and metasurface imaging," *Infrared and Laser Engineering,* vol. 50, no. 12, pp. 20211058-1-20211058-12, 2021.
[15] N. Shlezinger, G. C. Alexandropoulos, M. F. Imani, Y. C. Eldar, and D. R. Smith, "Dynamic metasurface antennas for 6G extreme massive MIMO communications," *IEEE Wireless Communications,* vol. 28, no. 2, pp. 106-113, 2021.
[16] H. Zhang, N. Shlezinger, F. Guidi, D. Dardari, M. F. Imani, and Y. C. Eldar, "Beam focusing for near-field multi-user MIMO communications," *IEEE Transactions on Wireless Communications,* 2022.
[17] D. M. Sheen, A. M. Jones, and T. E. Hall, "Simulation of active cylindrical and planar millimeter-wave imaging systems," in *Passive and Active Millimeter-Wave Imaging XXI*, 2018, vol. 10634: SPIE, pp. 47-57.
[18] M. Abbasi, A. Shayei, M. Shabany, and Z. Kavehvash, "Fast Fourier-based implementation of synthetic aperture radar algorithm for multistatic imaging system," *IEEE Transactions on Instrumentation and Measurement,* vol. 68, no. 9, pp. 3339-3349, 2018.
[19] A. M. Molaei, R. Kumar, S. Hu, V. Skouroliakou, V. Fusco, and O. Yurduseven, "A Compressive Sensing-Based Approach for Millimeter-Wave Imaging Compatible with Fourier-Based Image Reconstruction Techniques," in *2022 23rd International Radar Symposium (IRS)*, 2022: IEEE, pp. 87-91.
[20] A. Randazzo *et al.*, "A two-step inverse-scattering technique in variable-exponent Lebesgue spaces for through-the-wall microwave imaging: Experimental results," *IEEE Transactions on Geoscience and Remote Sensing,* vol. 59, no. 9, pp. 7189-7200, 2021.
[21] A. M. Molaei, V. Skouroliakou, V. Fusco, and O. Yurduseven, "Efficient 3D Image Reconstruction for Near-Field Microwave Imaging Using Dynamic Metasurface Antenna," *IEEE Access,* vol. 10, pp. 68491-68498, 2022.
[22] L. Wang, L. Li, Y. Li, H. C. Zhang, and T. J. Cui, "Single-shot and single-sensor high/super-resolution microwave imaging based on metasurface," *Sci Rep,* vol. 6, no. 1, pp. 1-8, 2016.
[23] L. Pulido-Mancera *et al.*, "Application of range migration algorithms to imaging with a dynamic metasurface antenna," *JOSA B,* vol. 33, no. 10, pp. 2082-2092, 2016.
[24] A. V. Diebold, L. Pulido-Mancera, T. Sleasman, M. Boyarsky, M. F. Imani, and D. R. Smith, "Generalized range migration algorithm for synthetic aperture radar image reconstruction of metasurface antenna measurements," *JOSA B,* vol. 34, no. 12, pp. 2610-2623, 2017.
[25] T. M. Fortier *et al.*, "Generation of ultrastable microwaves via optical frequency division," *Nature Photonics,* vol. 5, no. 7, pp. 425-429, 2011.
[26] B. Nuss, J. Mayer, S. Marahrens, and T. Zwick, "Frequency comb OFDM radar system with high range resolution and low sampling rate," *IEEE Transactions on Microwave Theory and Techniques,* vol. 68, no. 9, pp. 3861-3871, 2020.
[27] A. M. Molaei, O. Yurduseven, and V. Fusco, "An efficient waveform diversity based on variational mode decomposition of coded beat-frequency shifted signals algorithm for multiple-input multiple-output millimetre-wave imaging," *IET Radar, Sonar & Navigation,* vol. 15, no. 10, pp. 1266-1280, 2021.
[28] A. M. Molaei, S. Hu, V. Fusco, and O. Yurduseven, "A multi-resolution analysis-based approach to accelerate data acquisition for near-field MIMO millimeter-wave imaging," in *Passive and Active Millimeter-Wave Imaging XXV*, 2022, vol. 12111: SPIE, pp. 90-101.
[29] T. Sleasman, "Dynamic metasurface apertures for computational imaging," Duke University, 2018.
[30] A. V. Diebold, "Coherence in Dynamic Metasurface Aperture Microwave Imaging Systems," Duke University, 2020.
[31] T. Sleasman, M. Boyarsky, M. F. Imani, J. N. Gollub, and D. R. Smith, "Design considerations for a dynamic metamaterial aperture for computational imaging at microwave frequencies," *JOSA B,* vol. 33, no. 6, pp. 1098-1111, 2016.
[32] T. A. Sleasman, M. F. Imani, A. V. Diebold, M. Boyarsky, K. P. Trofatter, and D. R. Smith, "Implementation and characterization of a two-dimensional printed circuit dynamic metasurface aperture for computational microwave imaging," *IEEE Transactions on Antennas and Propagation,* vol. 69, no. 4, pp. 2151-2164, 2020.
[33] D. R. Smith, O. Yurduseven, L. P. Mancera, P. Bowen, and N. B. Kundtz, "Analysis of a waveguide-fed metasurface antenna," *Physical Review Applied,* vol. 8, no. 5, p. 054048, 2017.
[34] A. M. Molaei *et al.*, "Development of Fast Fourier-Compatible Image Reconstruction for 3D Near-Field Bistatic Microwave Imaging with Dynamic Metasurface Antennas," *IEEE Transactions on Vehicular Technology,* 2022.
[35] G. Lipworth *et al.*, "Comprehensive simulation platform for a metamaterial imaging system," *Applied optics,* vol. 54, no. 31, pp. 9343-9353, 2015.
[36] T. Sharma, A. Chehri, and P. Fortier, "Reconfigurable Intelligent Surfaces for 5G and beyond Wireless Communications: A Comprehensive Survey," *Energies,* vol. 14, no. 24, p. 8219, 2021.
[37] A. de Lustrac, B. Ratni, G.-P. Piau, Y. Duval, and S. N. Burokur, "Tri-state metasurface-based electromagnetic screen with switchable reflection, transmission, and absorption functionalities," *ACS Applied Electronic Materials,* vol. 3, no. 3, pp. 1184-1190, 2021.
[38] T. V. Hoang *et al.*, "Spatial diversity improvement in frequency-diverse computational imaging with a multi-port antenna," *Results in Physics,* vol. 22, p. 103906, 2021.
[39] T. Fromenteze, D. Carsenat, and C. Decroze, "A precorrection method for passive UWB time-reversal beamformer," *IEEE Antennas and Wireless Propagation Letters,* vol. 12, pp. 836-840, 2013.
[40] T. Fromenteze, E. Kpre, D. Carsenat, and C. Decroze, "Clean deconvolution applied to passive compressed beamforming," *Progress In Electromagnetics Research C,* vol. 56, pp. 163-172, 2015.
[41] S. Albeverio and Z. Brzezniak, "Finite dimensional approximation approach to oscillatory integrals and stationary phase in infinite dimensions," *Journal of functional analysis,* vol. 113, no. 1, pp. 177-244, 1993.
[42] M. Born and E. Wolf, *Principles of optics: electromagnetic theory of propagation, interference and diffraction of light*. Elsevier, 2013.
[43] T. Fromenteze, O. Yurduseven, F. Berland, C. Decroze, D. R. Smith, and A. G. Yarovoy, "A transverse spectrum deconvolution technique for MIMO short-range Fourier imaging," *IEEE Transactions on Geoscience and Remote Sensing,* vol. 57, no. 9, pp. 6311-6324, 2019.
[44] H. Gao *et al.*, "Study of the extended phase shift migration for three-dimensional MIMO-SAR imaging in terahertz band," *IEEE Access,* vol. 8, pp. 24773-24783, 2020.
[45] J. Rebouças and P. Brandão, "Scattering of light by a parity-time-symmetric dipole beyond the first Born approximation," *Physical Review A,* vol. 104, no. 6, p. 063514, 2021.
[46] D. Van Orden and V. Lomakin, "Rapidly convergent representations for 2D and 3D Green's functions for a linear periodic array of dipole sources,"

IEEE transactions on antennas and propagation, vol. 57, no. 7, pp. 1973-1984, 2009.

[47] T. V. Hoang *et al.*, "Frequency Selective Computational Through Wall Imaging Using a Dynamically Reconfigurable Metasurface Aperture," *IEEE Open Journal of Antennas and Propagation,* vol. 3, pp. 353-362, 2022.

[48] I. Amiri, P. Kuppusamy, A. N. Z. Rashed, P. Jayarajan, M. Thiyagupriyadharsan, and P. Yupapin, "The engagement of hybrid ultra high space division multiplexing with maximum time division multiplexing techniques for high-speed single-mode fiber cable systems," *Journal of Optical Communications,* vol. 43, no. 2, pp. 219-223, 2022.

[49] I. Kyrchei, "Analogs of Cramer's rule for the minimum norm least squares solutions of some matrix equations," *Applied Mathematics and Computation,* vol. 218, no. 11, pp. 6375-6384, 2012.

[50] I. Kyrchei, "Explicit representation formulas for the minimum norm least squares solutions of some quaternion matrix equations," *Linear Algebra and its Applications,* vol. 438, no. 1, pp. 136-152, 2013.

[51] G. Gao and C. Torres-Verdín, "High-order generalized extended Born approximation for electromagnetic scattering," *IEEE Transactions on Antennas and propagation,* vol. 54, no. 4, pp. 1243-1256, 2006.

[52] J. M. Lopez-Sanchez and J. Fortuny-Guasch, "3-D radar imaging using range migration techniques," *IEEE Transactions on antennas and propagation,* vol. 48, no. 5, pp. 728-737, 2000.

[53] Z. Wang, Q. Guo, X. Tian, T. Chang, and H.-L. Cui, "Near-field 3-D millimeter-wave imaging using MIMO RMA with range compensation," *IEEE Transactions on Microwave Theory and Techniques,* vol. 67, no. 3, pp. 1157-1166, 2018.

[54] A. M. Molaei, P. del Hougne, V. Fusco, and O. Yurduseven, "Efficient Joint Estimation of DOA, Range and Reflectivity in Near-Field by Using Mixed-Order Statistics and a Symmetric MIMO Array," *IEEE Transactions on Vehicular Technology,* vol. 71, no. 3, pp. 2824-2842, 2021.

[55] A. M. Molaei, P. Del Hougne, V. Fusco, and O. Yurduseven, "Numerical-Analytical Study of Performance of Mixed-Order Statistics Algorithm for Joint Estimation of DOA, Range and Backscatter Coefficient in a MIMO Structure," in *2022 23rd International Radar Symposium (IRS)*, 2022: IEEE, pp. 396-401.

[56] A. M. Molaei, S. Hu, V. Skouroliakou, V. Fusco, X. Chen, and O. Yurduseven, "Fast processing approach for near-field terahertz imaging with linear sparse periodic array," *IEEE Sensors Journal,* vol. 22, no. 5, pp. 4410-4424, 2022.

[57] J. C. Mello Román, J. L. Vázquez Noguera, H. Legal-Ayala, D. P. Pinto-Roa, S. Gomez-Guerrero, and M. García Torres, "Entropy and contrast enhancement of infrared thermal images using the multiscale top-hat transform," *Entropy,* vol. 21, no. 3, p. 244, 2019.

[58] Y. Meng, C. Lin, A. Qing, and N. K. Nikolova, "Accelerated Holographic Imaging With Range Stacking for Linear Frequency Modulation Radar," *IEEE Transactions on Microwave Theory and Techniques,* vol. 70, no. 3, pp. 1630-1638, 2021.

[59] W. Shuzhen, F. Yang, Z. Jin'gang, L. Mingshi, and L. Qing, "Near-field 3D imaging approach combining MJSR and FGG-NUFFT," *Journal of Systems Engineering and Electronics,* vol. 30, no. 6, pp. 1096-1109, 2019.